

Supplemental Material for
General-purpose neural network interatomic potential for the α -iron and
hydrogen binary system: Toward atomic-scale understanding of hydrogen
embrittlement

Fan-Shun Meng

*Department of Mechanical Science and Bioengineering, Osaka University,
1-3 Machikaneyama, Toyonaka, Osaka, Japan 560-8531. and
School of Science, Liaoning University of Technology, Jinzhou, China 121001.*

Jun-Ping Du

*Center for the Element Strategy Initiative for Structural Materials (ESISM),
Kyoto University, Sakyo-ku, Kyoto, Japan 606-8501. and
Department of Mechanical Science and Bioengineering, Osaka University,
1-3 Machikaneyama, Toyonaka, Osaka, Japan 560-8531.*

Shuhei Shinzato and Peijun Yu

*Department of Mechanical Science and Bioengineering, Osaka University,
1-3 Machikaneyama, Toyonaka, Osaka, Japan 560-8531.*

Hideki Mori

Department of Mechanical Engineering, College of Industrial Technology, Hyogo, Japan 661-0047.

Kazuki Matsubara and Nobuyuki Ishikawa

Steel Research Laboratory, JFE Steel Corporation, Kawasaki, Japan 210-0855.

Shigenobu Ogata

*Department of Mechanical Science and Bioengineering, Osaka University,
1-3 Machikaneyama, Toyonaka, Osaka, Japan 560-8531. and
Center for the Element Strategy Initiative for Structural Materials (ESISM),
Kyoto University, Sakyo-ku, Kyoto, Japan 606-8501.*

SI. DETAILS OF THE REFERENCE DATABASE AND SUMMARIZATION OF TEST RESULTS ²

The complete reference database comprises three subsets of atomic structures and their corresponding energy and force data. The first subset (i) includes the data of pure α -iron prepared by the strategy used for constructing the machine learning potential of α -iron[1]. The second subset (ii) comprises the data of H atoms and clusters, and the third subset (iii) contains the data of systems of α -iron with H.

Subset (i) (1) Tensile and shear deformation, and volume expansion of $\pm 2.5\%$ and 0% in the α -iron supercell, respectively.

(2) Monovacancy to quadravacancy-complexes with various configurations.

(3) Self-interstitial atoms (SIA) with various configurations.

(4) Low index surfaces including (001), (110), (111), (112), (210), and (310).

(5) γ -surface for (110) and (112) planes.

(6) Atomic clusters with one to four atoms, Bain path.

(7) Transition states in the monovacancy diffusion pathway,

(8) Symmetric tilt GBs with tilt axes of $\langle 001 \rangle$ $\langle 110 \rangle$ and $\langle 111 \rangle$.

(9) Dislocation structures.

(10) Inherent structures in the liquid state.

Subset (ii) (11) Isolated H atom, H_2 molecule, H_2+H cluster and $H_2 + H_2$ cluster, H_2 molecular clusters.

Subset (iii) (12) H atoms in the structures of the above (1), (2), (4), (8), H_2 molecule above the surfaces in the structures of (4), and H atoms in a nano-void with 9-vacancy.

(13) H atoms in the structures of (7) and (9).

Considering the vibrational properties, *Ab-initio* MD (AIMD) simulations were conducted for the configurations in the structures of (1)–(5), (8), (9) and (11)–(13). Atomic coordinate constraints were imposed on some atoms in the structures of (13) to sustain their characteristic configurations in AIMD samplings. Details of AIMD calculations are listed in the Table S1 and Table S2 below. The summarization of the test results is tabulated in Table S3.

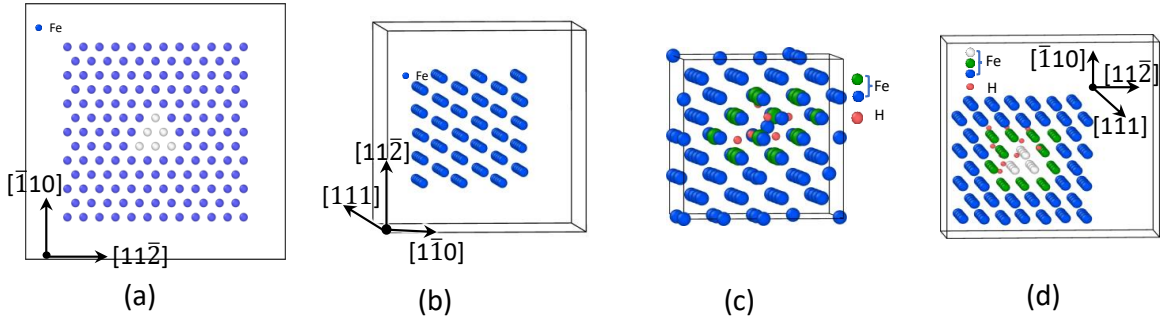


FIG. S1. Models mentioned in Table S1 and Table S2. (a) Supercell used for the screw dislocation straight pathway from Easy core configuration to a neighbouring easy-core configuration, from hard-core configuration to split-core configuration. The white balls stand for a hard-core configuration (for instance). Periodic condition was employed in all directions. The model thickness in the $[111]$ direction is $1b$, b is the burgers vector of bcc-iron. SCF calculations are conducted only, (b) Atomic structure for edge and vertex, (c) Atomic structure of vacancy transition state with nH . Coordinates of blue balls are fixed; red and olive balls are free, (d) A piece of pillar containing a screw dislocation at center. There is no vacuum slab in the $[111]$ direction. Coordinates of blue balls are fixed while others are free.

The architecture of feed-forward neural network used in this work is shown in Fig. S2:

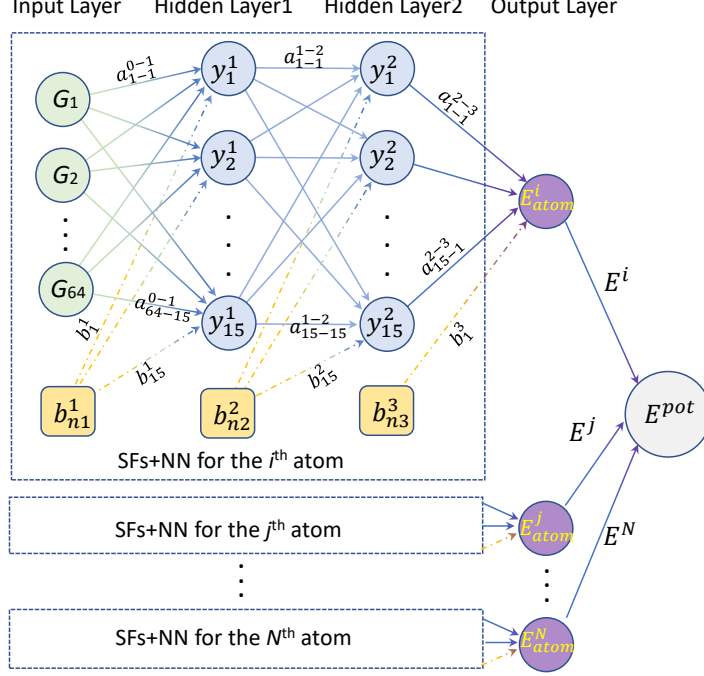


FIG. S2. Architecture of the feed-forward neural network. The part encircled by rectangular (symmetry functions and neural network) can produce the contribution of that atom to the potential energy of the system and should be applied for each atom in the system. The symmetry functions and NN architecture are set the same for the same element, while they can be different between different elements.

As reported in Ref. [2, 3], both potential energy of system and forces on each atom are functions of weights. The energies and forces are treated as independent pieces of information and randomly select whether weights update is based on an energy or a force component. The weight for the weights(fitting parameters) updating based on energy or on force. Here, we set the force update weight is 0.023. This information can be found in the potential file of *input.nn* (<https://github.com/mengfsou/NNIP-FeH>).

SIII. OVERFITTING DOUBLE CHECK

To ensure the avoiding of the overfitting issue, we prepared an independent dataset for validation by performing AIMD simulations for systems of H-vacancy, H-grain boundary, and H-surface at 800K. The initial structure of each AIMD simulation is a snapshot taken from AIMD simulations at 300K, which has been included in the reference database. AIMD simulations were also performed for twist GB and H-twist GB at 300K and 800K to enrich the variety of the validation dataset. Totally, 3240 configurations were prepared. Using the constructed NNIP to produce the root mean square errors (RMSE) of energy and force, and the results are presented in Fig. S3.

As shown in Fig. S3, the independent validation dataset has RMSE(E) and RMSE(F) of 2.52 meV/atom and 62.89 meV/Å, respectively. Comparing with the results in Fig. 1 in main text, these RMSEs can present the correct trend, specifically, the perfect match of energy. We now can confidently confirm that there is no serious overfitting occurred of the constructed NNIP.

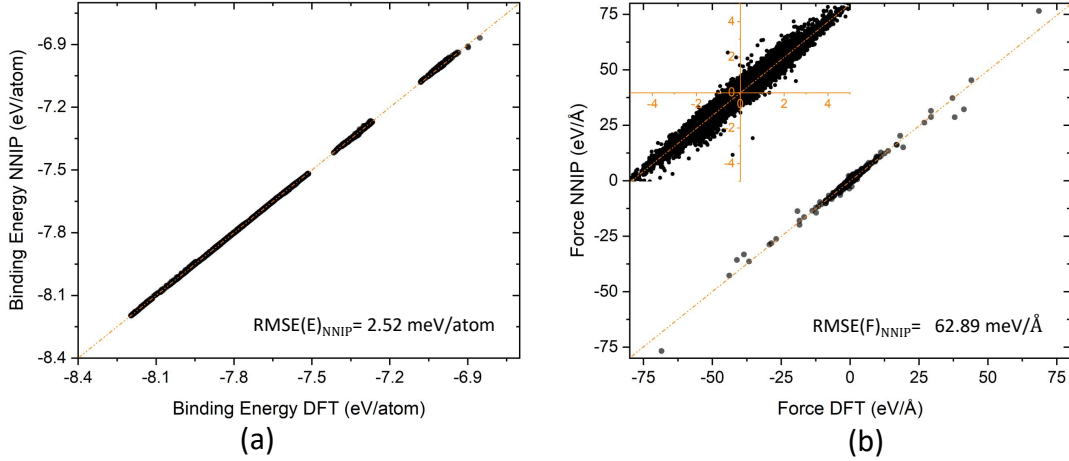


FIG. S3. Comparison of DFT and NNIP energies and forces of structures in the new prepared validation dataset. The line with a slop of 1 corresponds to a perfect training.

SIV. PERFORMANCE FOR PURE α -IRON

Based on the constructed NNIP, the basic properties of pure α -iron including lattice constant(a_0), elastic constants(C_{ij}) are printed in Table S4. As compared with DFT results, they are well reproduced. secondly, the formation energies of vacancy clusters are also presented. The notation for di-vacancy is based on nearest neighbors(NN) for the relative positions of the two vacancies, while that for the tri-vacancy are identified by means of Beeler notation[4]. $E_{4V-[111]}^f$ and E_{4V-Tet}^f for quad-vacancy, respectively, indicate the formation energies of 4 vacancies arranged along $[111]$ crystal direction and in tetrahedral configuration. Both of the ground states for tri-vacancy and quad-vacancy have compact configurations, which agrees with DFT results[5, 6]. For the case of self-interstitial, NNIP predicted that the configuration with dumbbell in $[110]$ direction is energetically preferred, which formation energy is 0.7 and 1.0 eV, respectively, lower than the dumbbells in $[100]$ and $[111]$ directions. This predication meets the DFT results very well[7, 8]. The free surface energies for low index surfaces of (001),(110)(111) and (112) are printed in the final column of Table S4. They show good agreement with DFT results in both qualitative and quantitative.

Note that, the data regarding the properties in Table S4 are all included in the reference database. The the reference data for vacancy clusters formation energies which are filled with "-" in the DFT column in Table S4, was prepared by AIMD only. The 4-vacancy case were calculated by DFT which is used to be compared with NNIP result.

The Bain path was calculated using a two-atom BCC unit cell by varying c/a ratio from 1.0 (BCC) to $\sqrt{2}$ (FCC) and the volume of cell was kept. As shown in Fig. S4(a), NNIP can well reproduce the Bain path. We also calculated the energy-volume (E-V) relations for crystalline structures of BCC, FCC, HCP and SC. As shown in Fig. S4(b), the E-V relations for BCC can be perfectly reproduced and for HCP, FCC and SC can be reasonably predicted with NNIP. There is no data referring HCP, FCC and SC phases in the reference database. The linear thermal expansion, $\Delta L/L$, can be obtained by straight MD simulation under various temperatures, which is shown and compared with available experimental results[15] in Fig. S4(c). It turns out that the experimental thermal trend is well reproduced above 200 K. It perfectly matches experimental results at 200 – 400 K, while it slightly underestimates at high temperature above 500 K. This little deviation might due to the GGA-PBE functional adoption in reference database generation[16, 17]. The significant discrepancy at low temperature is believed to be contributed by the quantum effect[18]. Beyond the grain boundary formation energy for $\langle 110 \rangle$ tilt axis described in main text, this NNIP also can properly predicate the formation energy of grain boundaries with tilt axes of $\langle 111 \rangle$ and $\langle 001 \rangle$ as shown and compared with available DFT results in Figs. S4(d) and (e). With the help of this NNIP, the surface energies with various orientations also can be properly obtained (not presented here), therefore, the constructed NNIP can predicted the seperation energy of various symmetric tilt grain boundaries. The γ -surface for $\{110\}$ crystallographic orientation reproduced with NNIP also vividly matches the DFT results reported in Ref.[1], as shown

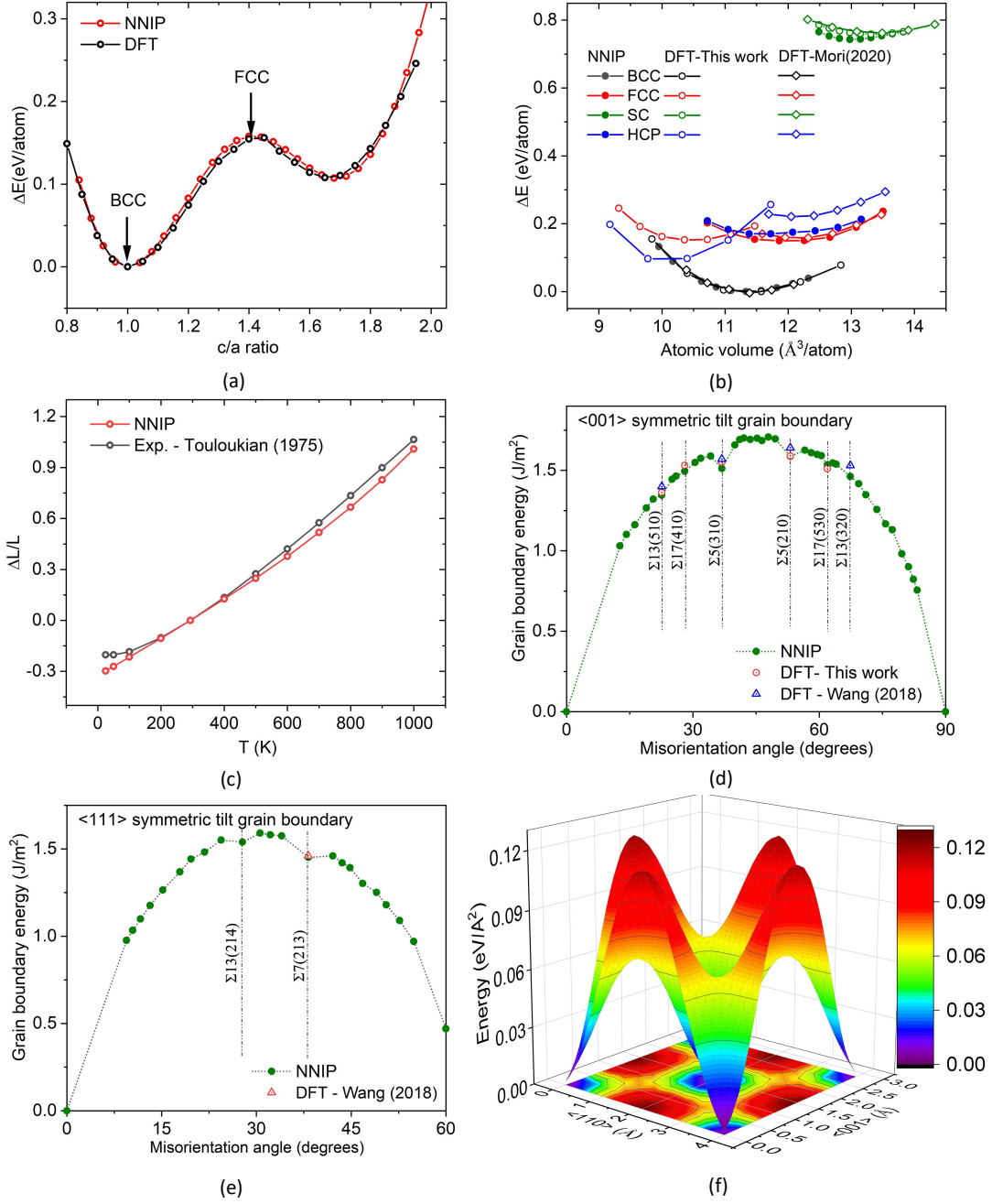


FIG. S4. Performance of NNIP for iron.(a) Bain path, (b) energy-volume relations for crystal lattice of bcc, fcc, hcp, sc of iron, (c)volume expansion under various temperature,(d)and (e) symmetric tilt GB misorientation-energy relationship for the (111) and (001) tilt axis, (f) gamma surface for the (110) crystallographic orientation, The available reported DFT[1, 9] and experimental[13] results for phonon dispersion curves, DFT[14] results for symmetric tilt GB formation energy, experimental results of thermal expansion relations[15] are also presented

in Fig. S4(f). Note that, the reference data for the properties in Fig. S4 are not all included in reference database, details are as following: For Figs. S4(a) and (f), all data are included in reference database (group (5) and (6) , the group number can be found in Sec.SI). For Fig. S4(b), only BCC phase data are included in reference database, FCC, SC, and HCP are not(group (1)). For Fig. S4(c), snapshots from AIMD simulations for BCC models at the temperatures of 300, 600, and 1000K are included in reference database(group (1)). The data included in the referece database has been marked in Fig. S4(d) and (e) (group (8)).

Screw dislocation glides along the $[11\bar{2}]$ direction in the $(1\bar{1}0)$ plane when a shear stress is exerted⁶ on the atoms in the upper and lower surfaces in opposite $\langle 111 \rangle$ directions (model of Fig. S5(a) was adopted in simulation). The gliding manner is consistent with the DFT analyses[19–23] and the classical theory[24] that the motion of screw dislocation is initiated by kink pair nucleation and the kinks move laterally along the dislocation line in the glide plane until the entire dislocation propagates to the next Peierls valley[25]. A movie of the kink pair nucleation at 200 K under a shear stress of 300 MPa is given in the Supplemental Materials (Mov. S1). The energy barriers of dislocation glide, that is dislocation glide speed, is strongly affected by the external applied stress[25]. Here, the stress dependent kink pair nucleation energy was further studied using the CI-NEB method. The kink pair nucleation energy at zero external stress is 0.70 eV, showing good agreement with that from the line tension (LT) model based on the DFT calculations of 0.73 eV[27] and 0.86 eV[26], although the kink pair nucleation energy is not included in the reference database. In addition, the kink pair nucleation energy under different external stresses is shown in Fig. S5(e).

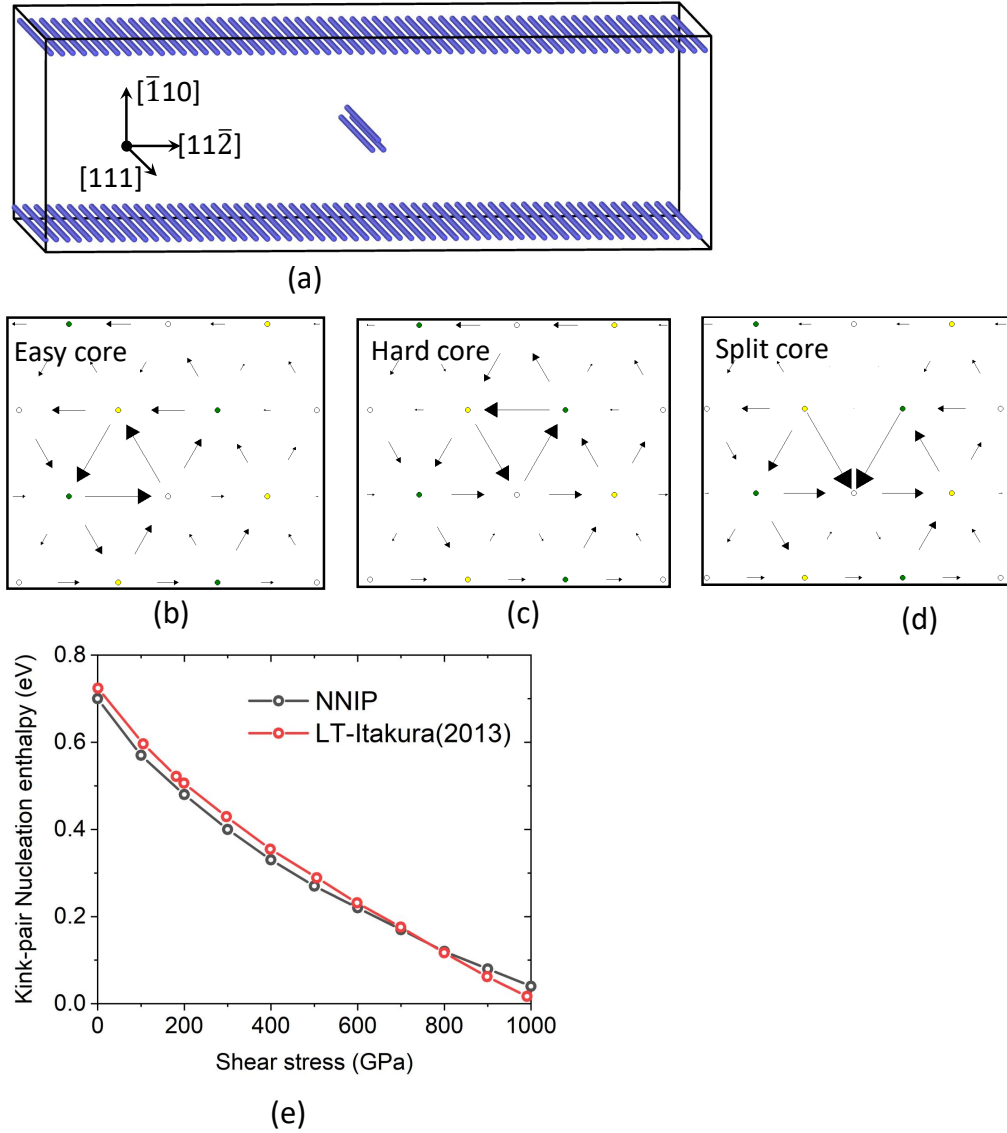


FIG. S5. (a) The model used for the study of screw dislocation gliding. (b)-(d) Differential displacement maps for easy core, hard core and split core configurations. (e) Shear stress dependence of kink nucleation enthalpy for screw dislocation. The result of the LT-DFT from Ref.[27] is also shown

The diffusivity of H in iron bulk was simulated for a supercell of $20a_0 \times 20a_0 \times 20a_0$ box containing 16,000 Fe atoms and 160 H atoms, the initial distribution of H atoms was randomly. The periodic boundary conditions were employed in all directions. Six temperatures were considered in this simulation: $T = 300, 400, 500, 600, 800$ and 1000 K. The system was relaxed at each temperature for 2.5 ps, followed by another 250 ps of data production. NPT ensemble and NVT ensemble with a timestep of 0.5 fs were adopted in relaxation and data production process respectively. The mean squared displacement (MSD) of H atoms were exported every 0.05 ps for further analysis. The diffusion coefficient of H atoms, D_H , can be calculated by the Einstein's equation as shown below:

$$D_H = \frac{1}{2 \times n_{\text{dim}}} \lim_{t \rightarrow \infty} \frac{d(\text{MDS})}{dt}, \quad (\text{S1})$$

where n_{dim} stands for the diffusion dimensionality, equivalent to 3 for this system. In order to obtain more accurate diffusivity for each temperature, the MSD for a given time interval is an average value for a trajectory segment with equal length but different start point in the trajectory. The calculated D_H at 300 K is $0.18 \times 10^{-8} \text{ m}^2/\text{s}$, which is less than that of experimental result of $0.87 \times 10^{-8} \text{ m}^2/\text{s}$ at 293 K [42]. This discrepancy is because the quantum effect is not taken into account in classical MD simulation and the quantum effects play a crucial role in the process of H migration at low temperature [43]. The calculated D_H at 1000 K is $2.545 \times 10^{-8} \text{ m}^2/\text{s}$, which agrees well with other classical MD simulations [44, 45] and experimental result [42]. We have to declare that the difference of chemical potential of a specific H concentration at various temperatures was neglected in all simulations. One can find the relation among concentration, temperature and chemical potential of H atom in iron bulk in Fig. S6(b).

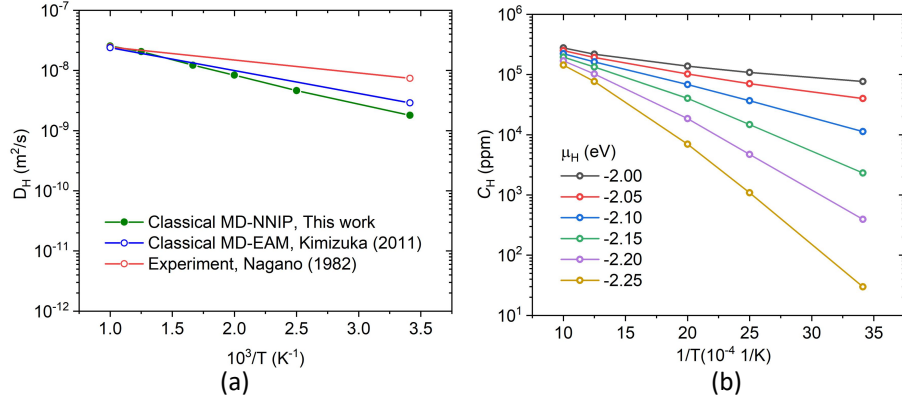


FIG. S6. (a). The H diffusivity in α -iron at various temperatures, the experimental result [42] and other classical MD simulation [43] are also presented. (b). The relation of chemical potential and the concentration of H in bulk iron at various temperatures.

SVI. SIZE DEPENDENCE OF HYDROGEN IN α -IRON

Fig. S7 show the energy and pressure decrease before and after the structure relaxation, $(\Delta E_{\text{rlx}}/\Delta P_{\text{rlx}})$, against the inverse of the number of atoms in supercell under the condition of volume fixing. Both ΔE_{rlx} and ΔP_{rlx} obtained with our NNIP are inversely proportional the system size and in reasonable quantitative agreement with DFT calculations [28]. This means our NNIP can apply for any size Fe-H systems.

Volumetric engineering-strain dependent E_s and ΔE were further tested, and the results are shown in Fig. S8. Comparing our results with those of reported DFT calculations [35], NNIP can correctly reproduce E_s in the considered strains. The ΔE predicated by NNIP is 0.092 eV at the strain of +2%, 0.108 eV at 0.0%, and 0.114 eV at -2%, which decreases with the volume expansion. However, the DFT results in Ref. [35] indicate that the barrier is almost independent of the applied volumetric strain; specifically, the barrier at the strain of 2% is slightly higher than that at 0%. To understand

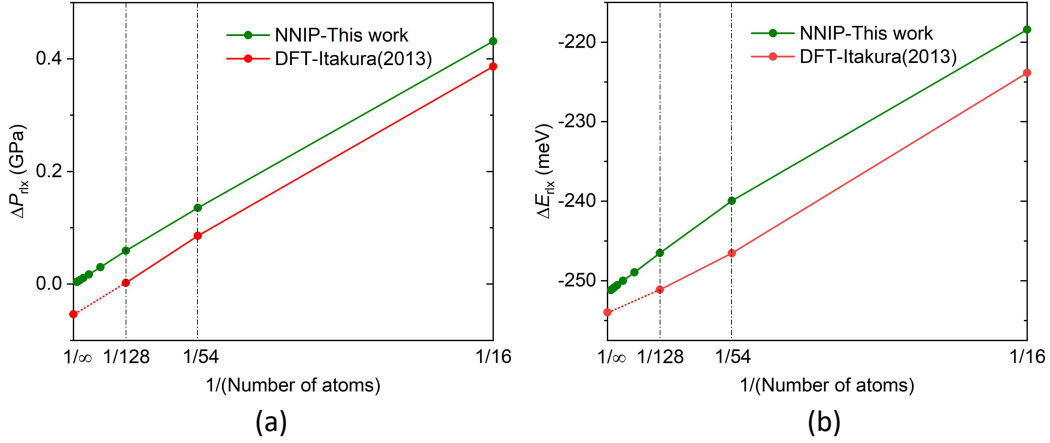


FIG. S7. Size dependence decrease of (a) energy and (b) pressure introduced by structure relaxation in the system of a bcc Fe bulk with an H atom at the T-site under the condition of volume fixed. The result of the DFT from Ref.[29] is also shown

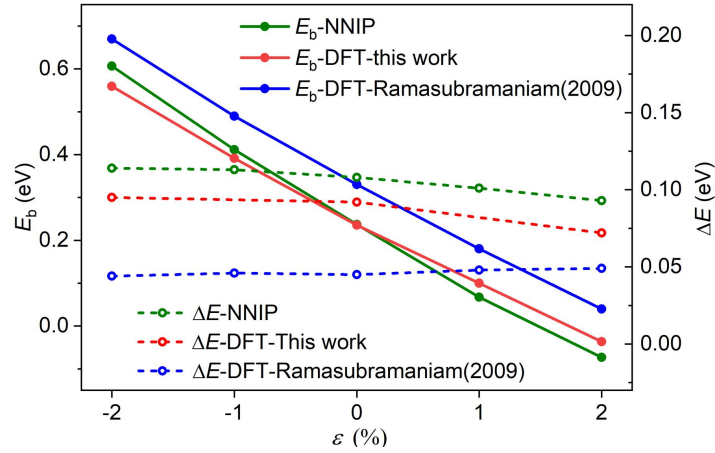


FIG. S8. Volumetric engineering-strain dependence of solution energy and diffusion barrier of H in bcc Fe bulk. DFT results extracted from Ref.[35] is also presented.

this disagreement, additional DFT CI-NEB calculations were performed for the structures with strains of $\pm 2\%$. The barrier of 0.092 eV at the strain of 0% decreased to 0.072 eV at +2% and increased to 0.095 eV at -2%, as shown in Fig. S8. Clearly, the barriers predicted by NNIP are in agreement with our DFT verifications. Disagreement might be introduced by the zero-point energy correction adopted in Ref.[35]. Note that the transition states of H atom diffusion between T-sites are included in the reference database, while the structures regarding the volumetric strain dependent ΔE are not.

SVII. CONFIGURATION AND ENERGETICS OF HYDROGEN IN MONOVACANCY

Instead of preferring T-site in bulk, hydrogen atom at a vacancy occupies a position slightly offset from an O-site neighboring the vacancy. The trapping energy for the i th H atom to a monovacancy is defined as:

$$E^{iH} = [E_{\text{Fe}+\text{H}}^{\text{bk}} - E_{\text{Fe}}^{\text{bk}}] - [E_{\text{Fe}+(i-1)\text{H}}^{\text{Va}} - E_{\text{Fe}+i\text{H}}^{\text{Va}}], \quad (\text{S2})$$

where $E_{\text{Fe}+i\text{H}}^{\text{Va}}$ is the energy of a system with a monovacancy and i H atoms. The trapping energy of a single H atom at monovacancy (E^{1H}) obtained with NNIP is 0.592 eV which agrees well with DFT obtaining, 0.575-0.616 eV, as listed in Table. S5. The displacement of H atom from the O-site towards

to the vacancy, as δH shown in Fig. S9, is 0.244 Å, which is more close to the DFT results of 0.224 Å[34], 0.23 Å[35] and 0.26 Å[37] than that of EAM results of 0.30 Å[35] and 0.39 Å[38].

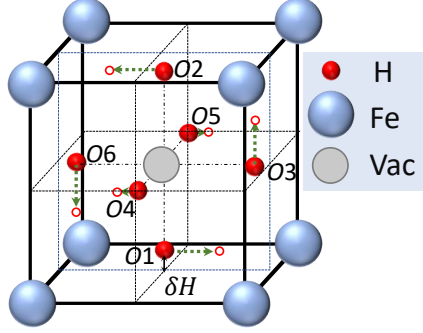


FIG. S9. Schematic of H-trapping sites at a monovacancy. δH is the distance from O1 to the nearest O-site. The arrows show the relative positions for the two configurations of 6 H atoms in vacancy, and the circles indicate its energetical favorable configuration

For multiple hydrogen atoms in a monovacancy, the sequence, which H atoms is assumed to be trapped, is labelled in Fig. S9. The trapping energies for different number of H atom at vacancy reproduced by NNIP agree well with other DFT results, as listed in Table S5. The configuration of 4 H atoms in vacancy prefers the tetrahedral arrangement (H atoms occupy O1-O4 sites in Fig. S9) rather than the planer arrangement (H atoms occupy O1,O2,O4 and O5 sites), which has been confirmed previously [6, 37]. The trapping energy of the former one is about 0.06 eV lower than the later one, which also agree with DFT obtaining of 0.1 [6] and 0.07 eV [37]. There are two configurations for 6 H atoms in vacancy and NNIP can describe both of them properly. The energetically favorable configuration has 2 hydrogen atoms at opposing O-sites while the other 4 hydrogen atoms at T-sites in one plane, as shown by red circles in Fig. S9. The above configuration can be obtained by relaxing the configuration with all H atoms near O-sites. The displacement of each atom in relaxation is shown by arrows in Fig. S9. Specifically, the displacement of H atoms occupied the opposing O-sites, *i.e.* O4 and O5, is 0.06 Å in opposite directions which agrees well with DFT results of 0.052 Å[37]. The trapping energies obtained with EIPs are also listed in Table S5.

SVIII. ADSORPTION OF HYDROGEN ON LOW INDEX SURFACES OF α -IRON

A slab with one hydrogen atom at the equivalent site on each terminates is used to calculate the adsorption energy. Therefore, the adsorption energy for H atom on the surface of (hkl), $E_{\text{ads}}^{\text{hkl}}$, can be obtained by:

$$E_{\text{ads}}^{\text{hkl}} = (E_{\text{slb}+2\text{H}}^{\text{hkl}} - E_{\text{slb}}^{\text{hkl}} - E_{\text{H}_2})/2, \quad (\text{S3})$$

where $E_{\text{slb}+2\text{H}}^{\text{hkl}}$ and $E_{\text{slb}}^{\text{hkl}}$ indicate the energy of the slab with and without H atoms. The benchmark of the energy of H-component is gaseous H_2 molecule, however, it is also represented by the atomic energy of an isolated hydrogen atom[41], E_{H} , Equ.S3 can be rewritten as following:

$$E_{\text{ads}}^{\text{hkl}} = (E_{\text{slb}+2\text{H}}^{\text{hkl}} - E_{\text{slb}}^{\text{hkl}} - 2 * E_{\text{H}})/2, \quad (\text{S4})$$

The results obtained by Equ. S4 will be only listed in Table. S6 for easy comparison with literature. The reproduced adsorption energy of H atom at hollow and bridge sites of (001) surface is -0.452 and -0.326 eV respectively, which correctly meets the results obtained by DFT that the hollow site is favored by 0.120 eV over bridge site[35]. For the structural aspect, the reproduced distances of H atom at hollow and bridge sites of (001) surface are 0.373 and 1.067 Å respectively, which agree well with the reported DFT result of 0.37 and 1.2 Å[35]. The corresponding distances by EAM potential are 0.20 and 0.74 Å[28]. For the case of (110) surface, the adsorption energy and the distance of H atom at the threefold site to surface is 0.776 eV and 0.998 Å, also show well agreement with DFT results of 0.70 eV and 0.98 Å[28]. For other surfaces, the energetical favorable adsorption site is threefold or semi-threefold site, the adsorption energies are listed and compared with available DFT results in

Table S6. As expected, NNIP predicts the reasonable adsorption energies for all tested surfaces. The adsorption energies produced by one of EAMs[36] are also listed in Table S6.

SIX. HYDROGEN EFFECT ON GB DECOHESION

Next, we test the NNIP performance in characterizing the influence of hydrogen on GB decohesion, which is not included in the reference database. First, the formation energy of GB (γ_{GB}) and segregation energy of H atom (γ_{seg}) in $\Sigma 5$ GB were calculated; their definitions can be found elsewhere[30–33]. As plotted in the upper panel of Fig. S10, GB formation energy decreases with increasing H atoms at the GB plane, indicating that the H-segregation stabilized GB. The middle panel of Fig. S10 shows that the hydrogen segregation energy is slightly reduced along with an increase in segregated H atoms. GB might accommodate more H atoms because of the negative segregation energy even when s1 sites are saturated. Both quantities quantitatively agree with the reported DFT results[30]. It is important to note that the H atoms were only set at s1 and other three equivalent sites at GB1. The work of separation of H-free GB (γ_{wos}^{H-free}) can be calculated as:

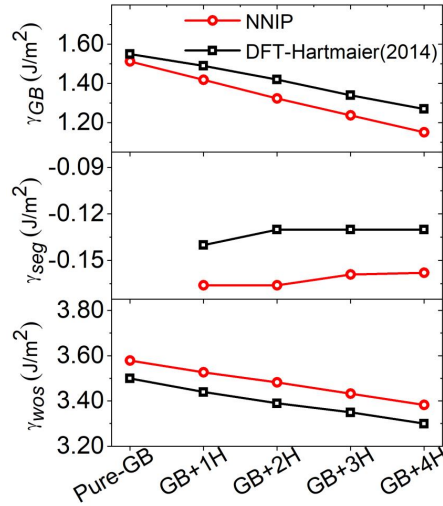


FIG. S10. Hydrogen segregation energy (γ_{seg}), GB formation energy (γ_{GB}), and the work of separation of clean and H-segregated GB (γ_{wos}). DFT results extracted from Ref.[30] are plotted, respectively.

$$\gamma_{wos}^{H-free} = (E_{grain-1} + E_{grain-2} - E_{GB})/2A, \quad (S5)$$

That for H-segregated GB (γ_{wos}^{H-seg}) is:

$$\gamma_{wos}^{H-seg} = (E_{grain-1+nH} + E_{grain-2} - E_{GB+nH})/A - \gamma_{wos}^{H-free}, \quad (S6)$$

where E_{GB+nH} and E_{GB} represent the energy of GB with and without H-segregation. $E_{grain-1+nH}$ and $E_{grain-1}$ are the energy of grain-1 with and without the segregated H atoms at the surface after GB separation. n is the number of H atom at GB1. $E_{grain-2}$ is the energy of grain-2 after GB separation. A is the cross-sectional area of the GB model. The pre-designed fracture path, grain-1, and grain-2 are identified in Fig. 4(a) in main text. The work required to separate H-free GB is 3.579 J/m². This value decreases with increasing the number of H atoms, reaching 3.382 J/m² when 4 H atoms are present at GB1. The segregation of hydrogen at GB slightly reduces the cohesion of GB, which is in excellent agreement with the DFT calculations[30], as shown in Fig. S10.

Typical diffusion trajectories of H atoms in a H-charging model with screw dislocation:

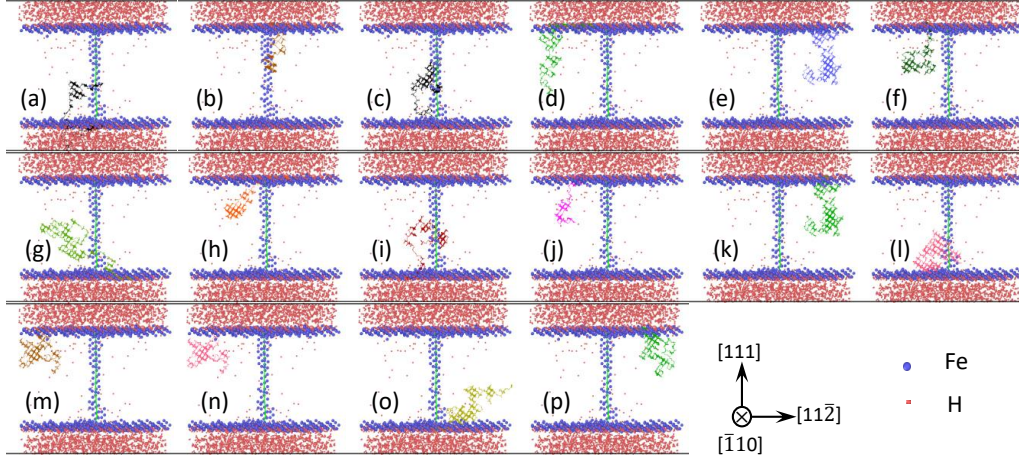


FIG. S11. Trajectories of H atoms in a model with screw dislocation. (a)-(c) involve the H diffusion along screw dislocation, (d)-(p) show the H atoms with random walk in bulk region.

SXI. H-TRAPPING AND DESORPTION AT DEFECTS

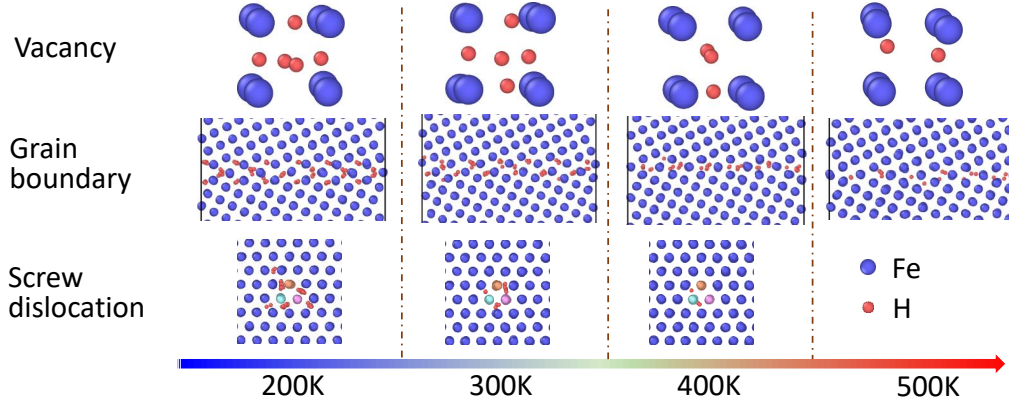


FIG. S12. Typical hydrogen distributions around defects of vacancy, grain boundary, and screw dislocation at various temperatures, the colored atoms for screw dislocation case stand for the dislocation core atoms.

- [1] Dragoni, D., Daff, T. D., Csányi, G. & Marzari, N. Achieving dft accuracy with a machine-learning interatomic potential: Thermomechanics and defects in bcc ferromagnetic iron. *Physical Review Materials* **2**, 013808 (2018).
- [2] Singraber, A., Morawietz, T., Behler, J. & Dellago, C. Parallel multistream training of high-dimensional neural network potentials. *Journal of Chemical Theory and Computation* **15**, 3075–3092 (2019).
- [3] Pukrittayakamee, A. *et al.* Simultaneous fitting of a potential-energy surface and its corresponding force fields using feedforward neural networks. *The Journal of chemical physics* **130**, 134101 (2009).
- [4] Beeler Jr, J. & Johnson, R. Vacancy clusters in α -iron. *Physical Review* **156**, 677 (1967).

- [5] Kandaskalov, D., Mijoule, C. & Connétable, D. Study of multivacancies in alpha Fe. *Journal of Nuclear Materials* **441**, 168–177 (2013).
- [6] Hayward, E. & Fu, C.-C. Interplay between hydrogen and vacancies in α -Fe. *Physical Review B* **87**, 174103 (2013).
- [7] Fu, C.-C., Willaime, F. & Ordejón, P. Stability and mobility of mono-and di-interstitials in α -Fe. *Physical Review Letters* **92**, 175503 (2004).
- [8] Marinica, M.-C., Willaime, F. & Mousseau, N. Energy landscape of small clusters of self-interstitial dumbbells in iron. *Physical Review B* **83**, 094119 (2011).
- [9] Mori, H. & Ozaki, T. Neural network atomic potential to investigate the dislocation dynamics in bcc iron. *Physical Review Materials* **4**, 040601 (2020).
- [10] Basinski, Z. S., Hume-Rothery, W. & Sutton, A. The lattice expansion of iron. *Proceedings of the Royal Society of London. Series A. Mathematical and Physical Sciences* **229**, 459–467 (1955).
- [11] Adams, J. J., Agosta, D., Leisure, R. & Ledbetter, H. Elastic constants of monocrystal iron from 3 to 500 K. *Journal of Applied Physics* **100**, 113530 (2006).
- [12] De Schepper, L. *et al.* Positron annihilation on pure and carbon-doped α -iron in thermal equilibrium. *Physical Review B* **27**, 5257 (1983).
- [13] Klotz, S. & Braden, M. Phonon dispersion of bcc iron to 10 GPa. *Physical Review Letters* **85**, 3209 (2000).
- [14] Wang, J., Madsen, G. K. & Drautz, R. Grain boundaries in bcc-Fe: a density-functional theory and tight-binding study. *Modelling and Simulation in Materials Science and Engineering* **26**, 025008 (2018).
- [15] Touloukian, Y. S. Thermal expansion: metallic elements and alloys. *Thermophysical Properties of Matter* **12** (1975).
- [16] Dragoni, D., Ceresoli, D. & Marzari, N. Thermoelastic properties of α -iron from first-principles. *Physical Review B* **91**, 104105 (2015).
- [17] Sha, X. & Cohen, R. Lattice dynamics and thermodynamics of bcc iron under pressure: First-principles linear response study. *Physical Review B* **73**, 104303 (2006).
- [18] Yokoyama, T. & Eguchi, K. Anharmonicity and quantum effects in thermal expansion of an invar alloy. *Physical Review Letters* **107**, 065901 (2011).
- [19] Ventelon, L., Willaime, F., Clouet, E. & Rodney, D. Ab initio investigation of the peierls potential of screw dislocations in bcc Fe and W. *Acta Materialia* **61**, 3973–3985 (2013).
- [20] Dezerald, L. *et al.* Ab initio modeling of the two-dimensional energy landscape of screw dislocations in bcc transition metals. *Physical Review B* **89**, 024104 (2014).
- [21] Wakeda, M. *et al.* Chemical misfit origin of solute strengthening in iron alloys. *Acta Materialia* **131**, 445–456 (2017).
- [22] Dezerald, L., Proville, L., Ventelon, L., Willaime, F. & Rodney, D. First-principles prediction of kink-pair activation enthalpy on screw dislocations in bcc transition metals: V, Nb, Ta, Mo, W, and Fe. *Physical Review B* **91**, 094105 (2015).
- [23] Edagawa, K., Suzuki, T. & Takeuchi, S. Motion of a screw dislocation in a two-dimensional peierls potential. *Physical Review B* **55**, 6180 (1997).
- [24] Seeger, A. Lxv. on the theory of the low-temperature internal friction peak observed in metals. *Philosophical Magazine* **1**, 651–662 (1956).
- [25] Shinzato, S., Wakeda, M. & Ogata, S. An atomistically informed kinetic monte carlo model for predicting solid solution strengthening of body-centered cubic alloys. *International Journal of Plasticity* **122**, 319–337 (2019).
- [26] Proville, L., Ventelon, L. & Rodney, D. Prediction of the kink-pair formation enthalpy on screw dislocations in α -iron by a line tension model parametrized on empirical potentials and first-principles calculations. *Physical Review B* **87**, 144106 (2013).
- [27] Itakura, M., Kaburaki, H. & Yamaguchi, M. First-principles study on the mobility of screw dislocations in bcc iron. *Acta Materialia* **60**, 3698–3710 (2012).
- [28] Itakura, M., Kaburaki, H., Yamaguchi, M. & Okita, T. The effect of hydrogen atoms on the screw dislocation mobility in bcc iron: a first-principles study. *Acta Materialia* **61**, 6857–6867 (2013).
- [29] Li, S. *et al.* The interaction of dislocations and hydrogen-vacancy complexes and its importance for deformation-induced proto nano-voids formation in α -Fe. *International Journal of Plasticity* **74**, 175–191 (2015).
- [30] Tahir, A., Janisch, R. & Hartmaier, A. Hydrogen embrittlement of a carbon segregated $\Sigma 5$ (310)[001] symmetrical tilt grain boundary in α -Fe. *Materials Science and Engineering: A* **612**, 462–467 (2014).
- [31] Huang, S., Chen, D., Song, J., McDowell, D. L. & Zhu, T. Hydrogen embrittlement of grain boundaries in nickel: an atomistic study. *npj Computational Materials* **3**, 1–8 (2017).
- [32] Geng, W., Freeman, A. J., Wu, R., Geller, C. & Reynolds, J. Embrittling and strengthening effects of hydrogen, boron, and phosphorus on a $\Sigma 5$ nickel grain boundary. *Physical Review B* **60**, 7149 (1999).
- [33] Všianská, M. & Šob, M. The effect of segregated sp-impurities on grain-boundary and surface structure, magnetism and embrittlement in nickel. *Progress in Materials Science* **56**, 817–840 (2011).
- [34] Tateyama, Y. & Ohno, T. Stability and clusterization of hydrogen-vacancy complexes in α -Fe: an ab initio study. *Physical Review B* **67**, 174105 (2003).

- [35] Ramasubramaniam, A., Itakura, M. & Carter, E. A. Interatomic potentials for hydrogen in α -iron based on density functional theory. *Physical Review B* **79**, 174101 (2009).
- [36] Wen, M. A new interatomic potential describing fe-h and hh interactions in bcc iron. *Computational Materials Science* **197**, 110640 (2021).
- [37] Hayward, E., Beeler, B. & Deo, C. Multiple hydrogen trapping at monovacancies. *Philosophical Magazine Letters* **92**, 217–225 (2012).
- [38] Wen, M., Xu, X.-J., Fukuyama, S. & Yokogawa, K. Embedded-atom-method functions for the body-centered-cubic iron and hydrogen. *Journal of Materials Research* **16**, 3496–3502 (2001).
- [39] Ohsawa, K., Eguchi, K., Watanabe, H., Yamaguchi, M. & Yagi, M. Configuration and binding energy of multiple hydrogen atoms trapped in monovacancy in bcc transition metals. *Physical Review B* **85**, 094102 (2012).
- [40] Song, J. & Curtin, W. Atomic mechanism and prediction of hydrogen embrittlement in iron. *Nature Materials* **12**, 145–151 (2013).
- [41] Wang, T. *et al.* Hydrogen adsorption structures and energetics on iron surfaces at high coverage. *The Journal of Physical Chemistry C* **118**, 4181–4188 (2014).
- [42] Nagano, M., Hayashi, Y., Ohtani, N., Isshiki, M. & Igaki, K. Hydrogen diffusivity in high purity alpha iron. *Scripta Metallurgica* **16**, 973–976 (1982).
- [43] Kimizuka, H., Mori, H. & Ogata, S. Effect of temperature on fast hydrogen diffusion in iron: A path-integral quantum dynamics approach. *Physical Review B* **83**, 094110 (2011).
- [44] Chen, Q., Yao, Q., Liu, Y.-L., Han, Q.-F. & Ding, F. Temperature-dependent dissolution and diffusion of H isotopes in iron for nuclear energy applications: First-principles and vibration spectrum predictions. *International Journal of Hydrogen Energy* **42**, 11560–11573 (2017).
- [45] Lu, T. *et al.* Molecular dynamics study of the diffusion properties of H in Fe with point defects. *Fusion Engineering and Design* **113**, 340–345 (2016).

TABLE S1. Details of the AIMD produced database for clean α -Fe

	Fe	T(K)	Total MD steps	Extraction1	Extraction2	Remarks
Phonon	3x3x3(0%, $\pm 2.5\%$) [$\pm 2.5\%$ expansion]	300	360		1/3	"1/3": 1 out of 3 are collected from all snapshots
		600	360		1/3	
		1000	360		1/3	
	3x3x3 (0%)	1400	214		1/3	
	4x4x4 (0%)	800	410		1/7	
	4x4x4 ($\pm 2.5\%$)	800	360		1/7	
liquid	4x4x4 (0%) - $\rightarrow \pm 2.0\%$	2000	360		1/20	Run MD without volume expansion. After that, pick some snapshots for expansion and shrinking, then SCF calculations.
1-Vacancy	3x3x3-1 (0%, $\pm 2.5\%$)	300	360		1/7	a 3x3x3 cell with 1 vacancy
		600	360		1/7	
		1000	360		1/3	
2-Vacancy	4x4x4-2(1NN)	800	360		1/7	
	4x4x4-2(2NN)	800	360		1/7	
	4x4x4-2(3NN)	800	360		1/7	
3-Vacancy	4x4x4-3(112)	800	205		1/4	
	4x4x4-3(113)	800	161		1/4	
	4x4x4-3(223)	800	136		1/4	
	4x4x4-3(333)	800	153		1/4	
4-Vacancy	4x4x4-4 (Tet)	800	211		1/5	
1-SIA	4x4x4-Tet [SIA at T-site]	100	229	1/1 (1-20)	1/10	"1/1 (1-20)": the first 20 snapshots are all collected, "1/10": 1 out of 10 are collected from the remaining snapshots
	4x4x4-Tet	300	363	1/1 (1-20)	1/10	
	4x4x4-Oct	100	219	1/1 (1-20)	1/10	
	4x4x4-(100)	100	360	1/1 (1-30)	1/3	SIA in (100) direction
	4x4x4-(100)	300	360	1/1 (1-20)	1/3	
	4x4x4-(110)	100	360	1/1 (1-20)	1/3	
	4x4x4-(110)	300	360	1/1 (1-20)	1/3	
	4x4x4-(110)	300	360	1/1 (1-20)	1/3	
2-SIA	4x4x4-(111)	300	175	1/1 (1-20)	1/3	
Low index surface	(110)	300	600		1/10	
	(111)	300	600		1/10	
	(210)	300	600		1/10	
	(310)	300	600		1/10	
	(112)	300	80	1/1 (1-30)	1/4	
γ -surface	(110), (112)	300	36		1/5	
Dislocation	screw-135 atoms (Dipole)	100	160	1/1 (1-20)	1/4	
		300	340		1/5	
	edge-180atoms	300	105		1/3	
	edge-135atoms	300	120	1/1 (1-20)	1/4	
	screw-dislocation (SCF)	0	150		1/1	See Fig. S2 (a)
Edge and vertex	{111}://{112} <110>	300	540	1/1 (1-20)	1/10	See Fig. S2 (b)
	{112}://{110} <111>	300	241	1/1 (1-20)	1/10	
	{111}://{110} <112>	300	470	1/1 (1-20)	1/10	
	{111}://{110}://{112}	300	230	1/1 (1-35)	1/5	
Grain boundary	$\Sigma 5$ (310)	300	600		1/10	
		600	600		1/10	
		1000	600		1/10	
	$\Sigma 5$ (210)	300	600		1/10	
		600	600		1/10	
	$\Sigma 3$ (112)	300	600		1/10	
		600	600		1/10	
	$\Sigma 3$ (111)	300	600		1/10	
		600	600		1/10	
		1000	600		1/10	

TABLE S2. Details of the AIMD produced database for H in α -Fe

	Fe	H	T(K)	Total MD steps	Extraction1	Extraction2	Remarks
H in bulk	2x2x2	1	300	30	1/1 (1-10)	1/10	
	3x3x3	1	300	297		1/10	
		2	300	160	1/1 (1-20)	1/10	
		6	300	360	1/1 (1-20)	1/10	
		10	300	465	1/1 (1-20)	1/15	
H in Vac	3x3x3-2	10	300	200	1/1 (1-20)	1/10	
	4x4x4-1	1,2,3,7	300	110	1/1 (1-20)	1/10	
		4,5,6,8	300	100	1/1 (1-20)	1/10	
	4x4x4-3	1,2	300	120	1/1 (1-15)	1/5	
		3,4	300	115	1/1 (1-15)	1/5	
		5,8	300	110	1/1 (1-15)	1/5	
		12	300	105	1/1 (1-20)	1/10	
		16	300	100	1/1 (1-15)	1/5	
	4x4x4-4	1,3,5,10	300	150	1/1 (1-15)	1/5	
		15,20,24	300	140	1/1 (1-15)	1/5	
		23	300	123	1/1 (1-15)	1/5	
	V-Tran-state	2	300	60	1/1 (1-15)	1/5	See Fig. S2 (c)
		4	300	70	1/1 (1-15)	1/5	
		10	300	150	1/1 (1-15)	1/5	
		10	1000	450	1/1 (1-10)	1/10	
		5	1000	440	1/1 (1-30)	1/10	
		6	1000	218	1/1 (1-20)	1/10	
		7	1000	207	1/1 (1-20)	1/10	
		8	1000	208	1/1 (1-20)	1/10	
		10	500	230	1/1 (1-20)	1/10	
		5, 6,7, 8	500	245	1/1 (1-20)	1/10	
H in void	4x4x4-9	9	300	419	1/1 (1-30)	1/10	
		10	300	401	1/1 (1-30)	1/10	
		11	300	425	1/1 (1-30)	1/10	
		12	300	178	1/2(1-80)	1/5	
		14	300	181	1/1 (1-20)	1/5	
		26	300	245	1/1 (1-10)	1/5	all Fe fixed
		45	300	116	1/1 (1-30)	1/5	
H on surface	(100)	4	300	245	1/1 (1-12)	1/10	
		8	300	206	1/1 (1-15)	1/6	
		10	300	360	1/1 (1-15)	1/10	
		6	300	280	1/4 (1-17)	1/10	
		8	300	300	1/1 (1-20)	1/6	
		14	300	333	1/1 (1-20)	1/10	
		4,8	300	360		1/10	
		5	300	330		1/5	
		10	300	300		1/10	
		5, 24	300	360		1/10	
H in screw dislocation	dipole 135 Fe	7	300	220	1/2 (1-20)	1/5	
		11	300	230	1/2 (1-20)	1/5	
		21	300	225	1/2 (1-20)	1/5	
	part-sd 208 Fe	3,5,6, 10,12, 18	200	20		1/1	See Fig. S2 (d)

	Fe	H	T(K)	Total MD steps	Extraction1	Extraction2	Remarks
H in GBs	$\sum 5 (310)$ 120 Fe	5	300	202	1/1 (1-15)	1/5	H along GB
		9	300	176	1/1 (1-10)	1/5	
		10	300	119	1/1 (1-10)	1/5	
		5	300	166	1/1 (1-20)	1/5	H randomly
		7	300	205	1/1 (1-16)	1/10	
		9	300	186	1/1 (1-20)	1/10	
		12	300	148	1/1 (1-20)	1/5	
		16	300	138	1/1 (1-15)	1/5	
		26	300	164	1/1 (1-15)	1/5	
	$\sum 5 (310)$ tensile for 25% in normal direction	3	300	130	1/2 (1-30)	1/5	H randomly
		5	300	248	1/1 (1-15)	1/5	
		15	300	164	1/1 (1-10)	1/5	
		10	300	58	1/1 (1-10)	1/2	
	$\sum 5 (310)$ 40 Fe	19	300	74	1/1 (1-20)	1/5	H along GB
		2	300	400	1/2 (1-40)	1/10	
		3	300	320	1/2 (1-20)	1/10	
		4	300	400	1/2 (1-20)	1/10	
		5	300	300	1/2 (1-20)	1/10	
		6	300	400	1/2 (1-20)	1/10	H randomly
		4	300	310	1/2 (1-20)	1/10	
		5	300	300	1/2 (1-20)	1/10	
		6	300	300	1/2 (1-20)	1/10	
		7	300	310	1/2 (1-20)	1/10	
		8	300	290	1/2 (1-19)	1/10	
H ₂ molecule	22 H in 5.2 ³ Å ³		300	360	1/1 (1-15)	1/10	
	42 H in 5.6 ³ Å ³		300	360	1/2(1-50)	1/10	
	108 H in 7.5 ³ Å ³		300	360		1/5	

TABLE S3. Considered properties following the data source categories of fully included, partially included* and no included, and the test results are also listed

Property	Component	Fully Included	Partial included	No included	Data source	Test result
Constants	Lattice constant (T) elastic constants	•			(1), (10)	Table. S4
Vacancy cluster formation energy	Mono-vacancy to quat-vacancy		•		(2)	Table. S4
Self-interstitial energy	Self-interstitial energy	•			(3)	Table. S4
Surface energy	Low index surface energy	•			(4)	Table. S4
Phonon dispersion	Phonon dispersion	•			MD-(1)	Fig. 2(a)
γ -surface	γ -surface	•			(5)	Fig. 2(b), Fig. S4(f)
Grain boundary (GB)	Tilt symmetry GBs		•		(8)	Fig. 2(c), Fig. S4(d)-(e)
	Twist GBs			•	-	Fig. S3, Sec. IV.3
screw dislocation (SD)	Formation energy of various core configures	•			(9)	Fig. 2(d)
	2-D Peierls potentials		•		(9)	Fig. 2(d)
	Kink-pair nucleation energy under various shear stress			•	-	Fig. S5(e)
H in α -iron bulk	Solution energy at T/O sites	•			(12)	Fig. S8
	Formation energy at T site under volumetric strain			•	-	Fig. S8
	Diffusion barrier	•			(12) [H in (1)]	Fig. S8
	Diffusion barrier under various volumetric strain			•	-	Fig. S8
H-vacancy interaction	Various number of H in monovacancy	•			(12) [H in (1)]	Table. S5
	H-vacancy complex diffusion	•			(12) [H in (7)]	Fig. 3(a)
H-surface reaction	Binding energy of H atoms at low index surfaces	•			(12) [H in (4)]	Table. S6
	H ₂ molecule nucleation on surfaces		•		MD- (12) [H ₂ in (4)]	Fig. 3(b)
H-GBs interaction	Solution energy of H at GBs		•		MD-(12) [H in (8)]	Fig. 4(a)-(b)
	Diffusion of H across GB		•		MD-(12) [H in (8)]	Fig. 4(c)
	H effects on GB decohesion			•	-	Fig. S10
	Solution energy of H around dislocation		•		13 [H in (9)]	Fig. 5(a),(c)
H-SD interaction	H diffusion around dislocation			•	-	Fig. 5(b),(d)
	H effects on dislocation mobility			•	-	Fig. 5(f)
	H effects on γ -surface in $\langle 111 \rangle$ direction			•	-	Fig. 5(e)

*There is no exact same data in the dataset but includes similar data, see main text for details

TABLE S4. Properties of α -Fe produced by NNIP. Results are compared to DFT(from this work and reported literature) and other machine learning iron potentials.

	NNIP	DFT	Existing-DFT	EXP	ANN[9]	GAP[1]
Lattice Constant(\AA)						
a_0	2.830	2.830	2.834[1]	2.855[10]	2.836	2.834
Elastic constants(GPa)						
C_{11}	296	297	297[1]	239.5[11]	277	285.9
C_{12}	147	151	151[1]	135.7[11]	156	154.3
C_{44}	96	105	109[1]	120.7[11]	104	103.8
Vacancy cluster formation energy(eV)						
E_{1V}^f	2.203	2.223	2.22[1]	2.0[12]	2.287	2.26
E_{2V-1NN}^f	4.184	4.236	4.24[1]	-	4.071	4.41
E_{2V-2NN}^f	4.183	4.201	4.20[1]	-	3.813	4.30
E_{2V-3NN}^f	4.445	-	4.45[1]	-	4.581	4.55
E_{2V-4NN}^f	4.374	-	-	-	4.385	4.48
E_{2V-5NN}^f	4.378	-	-	-	4.307	4.47
E_{3V-112}^f	5.867	-	5.82[5]	-	-	6.19
E_{3V-226}^f	6.146	-	6.13[5]	-	-	6.38
E_{3V-223}^f	6.155	-	6.70[5]	-	-	6.35
E_{3V-115}^f	6.152	-	6.15[5]	-	-	6.47
E_{3V-113}^f	6.185	-	6.14[5]	-	-	6.59
E_{3V-333}^f	6.665	-	-	-	-	6.85
$E_{4V-[111]}^f$	8.114	8.182	-	-	-	-
E_{4V-Tet}^f	7.278	7.254	7.51[6]	-	-	-
Self-interstitial energy (eV)						
E_{i-T}^f	4.448	4.466	4.79[1]	-	4.871	4.75
E_{i-O}^f	5.322	5.279	5.58[1]	-	5.703	5.53
$E_{i-[110]}^f$	4.037	4.023	4.37[1]	-	4.350	4.21
$E_{i-[111]}^f$	4.744	4.579	5.13[1]	-	5.023	4.90
$E_{i-[001]}^f$	5.062	5.146	5.48[1]	-	5.603	5.47
Low index surface energy (J/m^2)						
$\gamma_{(001)}$	2.479	2.488	2.543[1]	-	2.538	2.547
$\gamma_{(110)}$	2.436	2.449	2.495[1]	-	2.474	2.499
$\gamma_{(111)}$	2.695	2.691	2.752[1]	-	2.719	2.756
$\gamma_{(112)}$	2.586	2.575	2.629[1]	-	2.623	2.612

TABLE S5. Trapping energies of E^{iH} , in eV, for multiple H atoms in a vacancy. Positive value means energetically favorable. Results from previous reported DFT calculations and reproduced by EIPs are also listed for comparison. The results for the cases of 4H and 6H with difference configuration are shown in parentheses, details can be found in text.

iH	NNIP	PAW-PBE[37]	PAW-GGA[39]	PAW-PBE[6]	EAM[36]	EAM[40]	EAM[35]
1H	0.592	0.584	0.575	0.616	0.608	0.600	0.600
2H	0.612	0.607	0.609	0.651	0.567	0.557	0.600
3H	0.364	0.384	0.400	0.381	0.394	0.317	0.423
4H	0.342(0.286)	0.343	0.343	0.367	0.331	0.012	0.354
5H	0.325	0.297	0.321	0.269	0.234	0.254	0.228
6H	0.046(-0.039)	-0.002	-0.002	0.013	0.142	0.080	0.121

TABLE S6. Adsorption energy E_{ads}^{hkl} in eV for hydrogen atoms on various low index surfaces. Results from previous reported DFT calculations and reproduced by EIP are also listed for comparison.

(hkl)	E_{ads}^{hkl} -equ.S3			E_{ads}^{hkl} -equ.S4		
	NNIP	DFT[41]	EAM[36]	NNIP	DFT[41]	EAM[36]
(001)	0.452	0.46	0.434	2.724	2.732	2.800
(110)	0.776	0.70	0.493	3.047	2.949	2.859
(111)	0.589	0.51	0.390	2.861	2.775	2.756
(112)	0.652	0.60	0.478	2.922	2.862	2.843
(210)	0.650	0.66	0.476	2.923	2.905	2.841
(310)	0.635	0.65	0.438	2.907	2.905	2.804